RESEARCH ARTICLE | JANUARY 30 2026

A UHV-compatible flow reactor for model catalytic reactions under realistic conditions combined with catalyst cluster synthesis

Ramin Shadkam ; Martin Limbach; Mohana V. Kante; Ajai R. L. Nilayam ; Christian Kübel ; Robert Kruk ; Horst Hahn

Rev. Sci. Instrum. 97, 013907 (2026)
https://doi.org/10.1063/5.0307891

Review of Scientific Instruments ARTICLE pubs.aip.org/aip/rsi

A UHV-compatible flow reactor for model catalytic reactions under realistic conditions combined with catalyst cluster synthesis

Cite as: Rev. Sci. Instrum. 97, 013907 (2026); doi: 10.1063/5.0307891
Submitted: 19 October 2025 • Accepted: 30 December 2025 •
Published Online: 30 January 2026

Ramin Shadkam,[1] Martin Limbach,[1] Mohana V. Kante,[1] Ajai R. L. Nilayam,[1] Christian Kübel,[1,2,3] Robert Kruk,[1] and Horst Hahn[1,4,a)]

AFFILIATIONS

[1] Institute of Nanotechnology (INT), Karlsruhe Institute of Technology (KIT), Karlsruhe, Germany
[2] Karlsruhe Nano Micro Facility (KNMFi), Karlsruhe Institute of Technology (KIT), Karlsruhe, Germany
[3] Department of Materials & Earth Sciences, Technical University of Darmstadt, Darmstadt, Germany
[4] Department of Materials Science and Engineering, University of Arizona, Tucson, Arizona 85721, USA

[a)] **Author to whom correspondence should be addressed:** horst.hahn@kit.edu

ABSTRACT

The study of model catalysts under complex reaction conditions needs to address several challenges, including high-sensitivity detection and accurate control of reaction pressure and temperature, while ensuring a contamination-free environment. Here, we developed an ultra-high vacuum (UHV)-compatible flow reactor designed to investigate model catalytic reactions. The reactor is integrated into an existing UHV system, which facilitates the synthesis of mass-selected clusters and their controlled deposition on model substrates. The combination of the flow reactor with the preparation system enables catalyst preparation, characterization, and testing without exposure to ambient conditions. The reaction cell features a dual-cup design with a reaction volume of less than 3 ml and is equipped with a near-infrared laser heater and a quadrupole mass spectrometer for continuous product analysis. The gas handling unit allows for the use of different gas mixtures flowing at various pressures through the reaction cell. The laser heating unit provides precise temperature regulation through programmable heating and cooling profiles. As a proof of concept, catalytic CO oxidation was studied on a Pt(110) single crystal and CeO_2-supported mass-selected Pt_{200} clusters. The results demonstrate distinct reactivity trends, activation temperatures, and hysteresis behavior, highlighting the reactor's functionality for detailed studies in model heterogeneous catalysis.

I. INTRODUCTION

Model catalysis plays a crucial role in uncovering the fundamental mechanisms of surface reactions by enabling experiments on well-defined systems under controlled conditions. These well-defined systems (e.g., single crystals, thin films, and nanostructured materials) provide the control needed to disentangle the influence of critical parameters, such as surface structure, particle size, chemical composition, and catalyst–support interaction, on catalytic behavior. By isolating specific structural and chemical features, these systems allow for a fundamental understanding of catalytic processes often obscured in complex technical catalysts.[1–6] Model catalysts offer a direct correlation between surface structure and reactivity, serving as a basis for the interpretation of reaction behavior under experimentally relevant conditions.[7]

While ultra-high vacuum (UHV) studies provide precise control over surface characteristics, they often fail to replicate pressure and chemical environments equivalent to realistic catalytic conditions. Many surface reactions exhibit remarkable differences in kinetics, surface reconstruction, and active-site populations when transitioning from UHV to ambient or near-ambient pressures.[8–12] This so-called "pressure gap" limits the direct translation of reaction-level understanding from idealized model systems to practical catalytic conditions. Bridging this gap requires an experimental setup capable of systematic investigation of the same catalyst under both UHV and realistic reaction environments. Such studies are

essential for identifying pressure-dependent effects, validating reaction pathways proposed from UHV studies, and ultimately building a holistic understanding of catalytic behavior under operating conditions.[13–16]

Owing to the well-defined reaction pathway and the availability of model catalyst systems, CO oxidation ($CO + 1/2\ O_2 \rightarrow CO_2$) is among the most extensively studied reactions in heterogeneous catalysis and surface science.[9,17] The relatively simple stoichiometry of CO oxidation makes it a suitable benchmark reaction for exploring fundamental processes, such as surface adsorption, reaction kinetics, and structure–activity relationships. As efforts continue to bridge fundamental studies with more realistic conditions, CO oxidation remains a robust platform for evaluating new instrumentation aimed at probing catalytic behavior.[18–20]

Various pioneering designs have enabled catalysis studies under pressures ranging from UHV to ambient pressures on low-surface-area model catalysts. The first efforts to develop a high-pressure cell (HPC) reactor compatible with UHV systems were initiated by Somorjai and co-workers in the 1970s.[21,22] Building on this concept, the entire chamber volume typically served as the reaction vessel, allowing *in situ* surface characterization under UHV conditions. At higher pressure ranges, the isolation of the catalyst in a dedicated reaction cell facilitated gas analysis using mass spectrometry, complemented by pre-reaction and post-reaction characterizations. Based on this foundational work, numerous reactor designs have since been introduced and tailored to accommodate specific reactions or experimental conditions. Notably, the groups of Chorkendorff and Rupprechter have developed various highly sensitive, UHV-compatible reactors that integrate sample preparation, *in situ* surface analysis, and gas analysis techniques.[4,8,11,13,14,23–26] More recently, Zhang *et al.* reported a quasi-closed reactor system for ammonia synthesis studies, employing a quartz glass capillary sniffer to confine the reaction volume at a pressure of 1 bar while maintaining compatibility with UHV analysis.[27]

Despite significant progress, all proposed designs exhibit inherent advantages and limitations. In static (batch-mode) reactors, the reaction volume is typically large, allowing for extended residence times of reactants on the catalyst surface, but at the cost of side reactions on other reactive components. In contrast, dynamic (flow-mode) reactors enable real-time kinetic monitoring of reaction products; thereby, they minimize undesired side reactions and more accurately represent realistic catalytic conditions. However, the operational pressure range is often constrained by the requirements of the gas detection system. Given the low number of active sites in model catalysts, an ideal dynamic reactor must fulfill several key criteria: (i) a small reaction volume to ensure sufficient sensitivity, (ii) efficient heating capable of reaching high temperatures, (iii) a safe and contamination-free handling environment, and (iv) a reliable and highly sensitive gas detection system.[4,24,27]

In this work, we present a newly developed UHV-compatible flow reactor designed for model catalyst studies, integrated with an existing cluster ion beam deposition (CIBD) system. The reactor features a dual-cup design with a small reaction volume (less than 3 ml, depending on the sample size), precise and sensitive temperature control, and a quadrupole mass spectrometer (QMS) for gas-phase analysis. This setup enables the deposition of mass-selected noble metal clusters onto various substrates, followed by clean UHV transfer to the reaction cell for catalytic testing and subsequent characterization using standard UHV techniques.

The following section describes the general layout of the experimental setup and the design principles of the reactor in detail. As a proof of concept, CO oxidation was investigated under various reaction conditions using a Pt(110) single crystal and oxide-supported mass-selected Pt clusters as model catalysts.

II. EXPERIMENTAL SETUP

A. System overview

An overview of the experimental setup is shown in Fig. 1. The UHV facility comprises several interconnected systems designed for the preparation, modification, and characterization of model catalysts. The main components include the following:

(1) **Cluster ion beam deposition (CIBD):** A custom-built system for the generation and deposition of mass-selected clusters from various metallic materials. The working principles of the CIBD system have been described in detail elsewhere.[28,29] Briefly, the metal atoms are sputtered using a DC-powered magnetron sputter head mounted in a cryogenic condensation tube, where they collide with a stream of He and Ar to form clusters of various sizes. Upon exiting the source into the UHV beamline, the cluster beam is accelerated by multiple sets of electrostatic lenses toward the 90° magnet bender, which separates the clusters based on their kinetic energies, which directly correlate with their mass. The mass-selected clusters are subsequently steered and decelerated to the required energy prior to deposition on a substrate. The system allows fine control over deposition parameters, such as impact energy and temperature, enabling precise tuning of the size, shape, coverage, and structure of the deposited clusters. This level of control facilitates the preparation of well-defined cluster configurations, including isolated clusters or porous/dense cluster-assembled films. This versatility makes it particularly suitable for preparing model catalyst samples.

(2) **Pulsed laser deposition (PLD):** A flexible thin-film deposition system equipped with a Coherent KrF excimer laser (248 nm) for target ablation, dual gas inlet lines for reactive or inert gas environments, a laser heating stage monitored by a pyrometer, and a kSA 400 RHEED system for *in situ* surface analysis. The PLD system supports the growth of oxide thin films (using both commercial and synthesized oxide targets) as a support material for noble metal clusters in various morphologies—epitaxial, nano-, and polycrystalline.

(3) **Central distribution hub:** A central distribution hub connects both CIBD and the catalytic chamber to the rest of the UHV facility. With a base pressure of $\sim 5 \times 10^{-8}$ mbar, the distribution chamber ensures safe and clean UHV-compatible sample transfer between deposition and testing systems.

(4) **X-ray photoelectron spectroscopy (XPS):** The surface characterization system, which can be accessed without exposure to ambient conditions from the distribution hub, is equipped with X-ray (Al Kα), ion, electron beam, and UV sources, along with a Specs HSA 3500 hemispherical analyzer. XPS

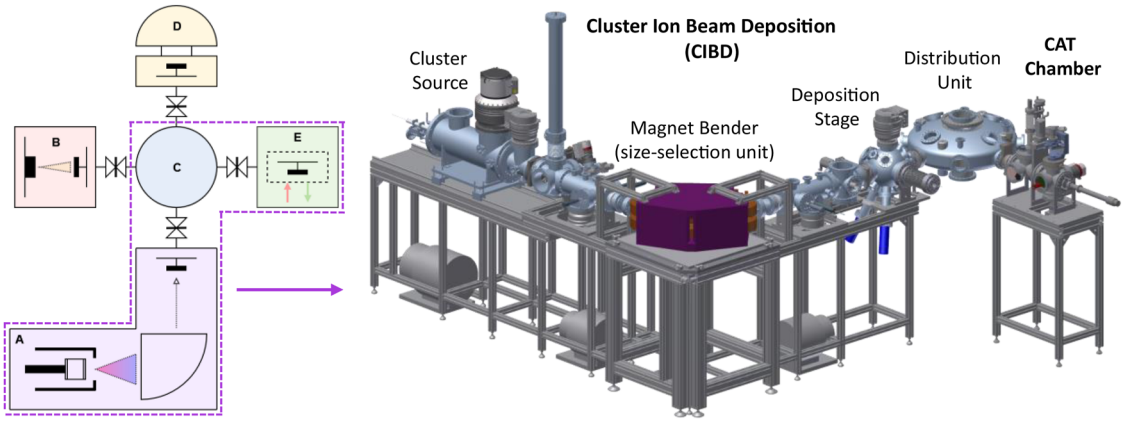

FIG. 1. Overview of the experimental setup: (left side) schematic of the UHV facility, including CIBD (A), PLD (B), central distribution hub (C), XPS (D), and CAT chamber (E); (right side) 3D CAD model of the CAT chamber integrated with the CIBD system via the central distribution hub.

is used to investigate the surface composition and elemental chemical states of thin films and clusters, quantify the deposited cluster coverage, and analyze the catalyst surface before and after reactions.

(5) **Catalytic chamber (CAT chamber):** A UHV-compatible reactor was explicitly developed for catalytic performance measurements under controlled reaction conditions. The integration of the CAT chamber with the existing UHV facility allows for a complete cycle of preparation, characterization, and performance testing of the model catalysts. Details of the technical components are described in the following section (B. Equipment design).

All modules operate as independent UHV units, each equipped with pumps and fast-entry load-locks, separated by gate valves, with base pressures ranging from the low 10^{-8} mbar range in the distribution hub and CAT chamber, to the low 10^{-9} mbar range in the PLD and XPS systems, and to the mid 10^{-10} mbar range in the CIBD. System accessibility is further enhanced via a central UHV transfer line that connects to additional deposition units (e.g., PLD) and pre-treatment systems for substrates (e.g., Ar^+ sputtering).

The integrated architecture of the facility enables a fully UHV-compatible workflow supporting pre-treatment, oxide support preparation, noble metal cluster deposition, and catalytic testing—all performed without exposing the sample to ambient conditions. This approach minimizes contamination risks and is critical for the reliable investigation of highly sensitive model catalyst systems.

B. Equipment design

Following the overview of the experimental setup, the key components of the CAT chamber are described in the following sections (1)–(4): the UHV-compatible reaction cell, the heating unit, the gas-handling and pumping system, and the gas analysis unit.

1. UHV-compatible reaction cell

Figure 2(a) presents the overall design of the CAT chamber. The left-hand-side chamber serves as a load-lock, allowing the reception of samples from CIBD via the distribution hub and the insertion of samples from outside. The load-lock can store up to eight samples. The load-lock operates as an intermediate chamber between the high-pressure reactor and the distribution hub, acting as a buffer to prevent vacuum loss in the event of a leak. The load-lock is equipped with a Pfeiffer HiPace 80 turbomolecular pump, a viewport, and a fast-entry access door.

The right-hand-side chamber, separated by a UHV gate valve, serves as the reaction chamber. The main feature of this chamber is the flow reactor located at its center. A magnetically coupled transfer arm, connected to a side flange, facilitates the transfer of samples from the load-lock to the reaction cell. On the top flange, an x–y–z manipulator positions the reaction cell at the center of the chamber, along with the fiber-optic feedthrough for the laser heating unit (described in Sec. II B 2). The multiport flange beneath the manipulator accommodates vacuum and absolute pressure gauges, an overpressure relief valve, and a UHV-tight leak valve. The leak valve, connected to inert gas (argon in this case), backfills the main reaction chamber. Its precise leak rate, combined with a gas-independent capacitive gauge, enables fine control of the chamber pressure. The gas-handling and pressure-sensing system is described further in Sec. II B 3.

The multiport flange at the bottom of the reaction chamber provides the gas inlet/outlet connections (CF16 flange to Swagelok fittings), a thermocouple feedthrough, and the turbomolecular pump, which can be isolated by a UHV gate valve. This gate valve allows separation of the pumping system while reactant gases flow through the chamber for measurement.

In Fig. 2(b), the detailed two-cup design of the reaction cell is shown. The upper cup is the moving part of the reactor, containing the sample-receiving stage and the laser heating unit. At the top, a hanger assembly connects the upper cup to the manipulator flange. The manipulator moves the upper cup along the z-axis to open and

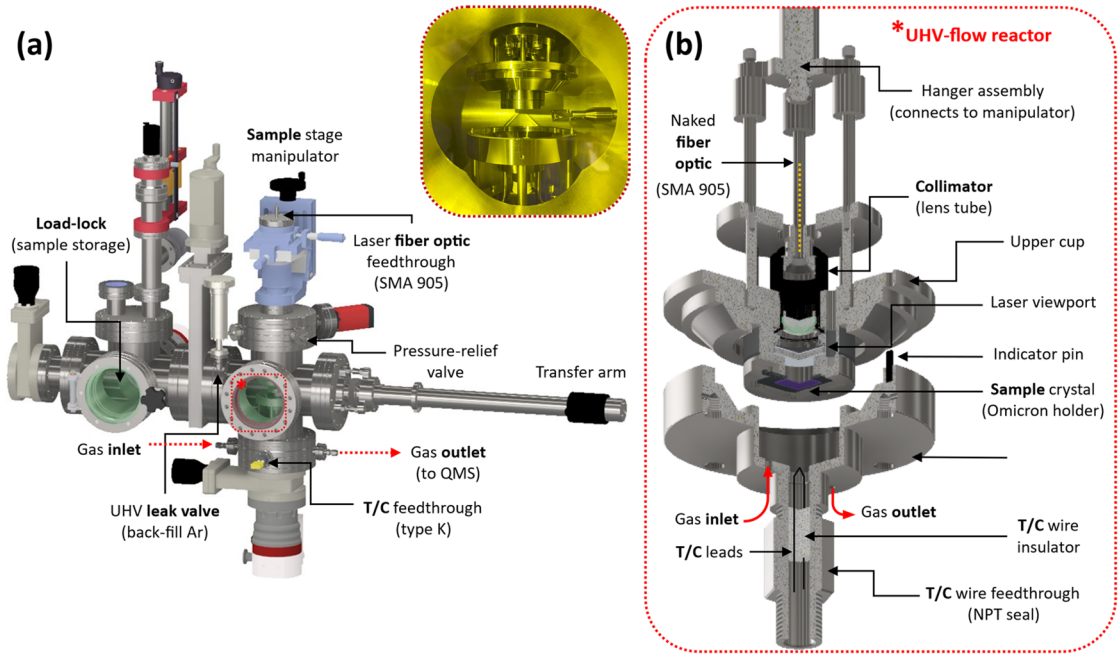

FIG. 2. 3D CAD model of the CAT chamber: (a) overall view and the main components of the CAT chamber (the inset displays a real image of the open reaction cell); (b) key components of the reaction cell in a cross-sectioned view.

close the cell, and along the x- and y-axes to ensure precise alignment of the upper cup with the lower, stationary cup. To close the cell correctly, two indicator pins on the lower cup must align with the corresponding holes on the upper cup.

The custom-designed conical geometry of the reaction cell provides reliable sealing. In this small-volume reactor (2.5 ml) with low gas flow, it is crucial that the gas reaches the sample and exits to the analyzer without leakage. To prevent leakage of reactant gases, a small force is applied using the manipulator when the cell is closed. In addition, before starting the experiment, the pressure in the main chamber is set slightly higher than the pressure inside the cell. The resulting isostatic pressure of the backfilled gas minimizes leakage from the cell to the main chamber. The backfill gas is chosen to match the carrier gas in the reaction mixture, so any minor flow from the main chamber into the cell does not affect the experiment.

In a typical experiment, the sample (mounted on a modified Omicron holder) is prepared in CIBD and transferred to the load-lock, where it can also be stored. The transfer arm places the sample in the receiving stage of the reaction cell, where the sample surface faces downward to contact a miniaturized type-K thermocouple. Heating is achieved by means of a laser beam striking the sample from the backside. At this stage, the sample in the open cell can be thermally cleaned in vacuum (or an inert gas atmosphere), oxidized, or reduced by backfilling the chamber with the appropriate gas. The cell is then closed by the vertical motion of the manipulator at the top, and a mixture of reactant gases, controlled by mass flow controllers (MFCs) in the gas manifold, flows into the cell and is pumped out through the outlet to the gas analyzer. This setup enables the catalytic testing of model samples over a wide pressure range and at temperatures from room temperature up to 1000 °C. Nevertheless, the case studies (catalytic CO oxidation) are conducted from room temperature up to 500 °C.

2. Heating unit

To minimize potential contamination from conventional resistive heaters and provide localized heating, a near-infrared laser is employed as the heating unit. Figure 3 illustrates the configuration of this unit. A customized laser unit with a diode-driven source (0–100 W) generates a 940 nm laser beam, which is guided through a 600 μm fused silica fiber optic. Due to the high laser output and to avoid energy loss at junctions, a one-piece fiber optic with a pigtail design (Wyoptics Co.) is used to transfer the beam from the source to the back of the sample.

On the atmospheric side, the laser beam couples to a 3 m long metal-armored patch cord connected to a CF16 flange feedthrough. On the vacuum side, the polyimide-coated fiber is attached to a lens collimator, which ensures that the beam spot heats only the sample crystal and not the surrounding components. Within the tube lens collimator, an aspheric condensing lens converges the beam to a ~5 mm diameter spot that matches the opening at the center of the sample holder. In this way, only the sample is heated, and, due to minimal thermal contact between the sample and the sample holder, heat transfer to the rest of the receiving stage is minimized. This configuration avoids the need for a cooling medium and eliminates background reactions on the surrounding metallic parts. For model catalysts with very few active sites, preventing background reactions is crucial for achieving reliable and precise measurements.

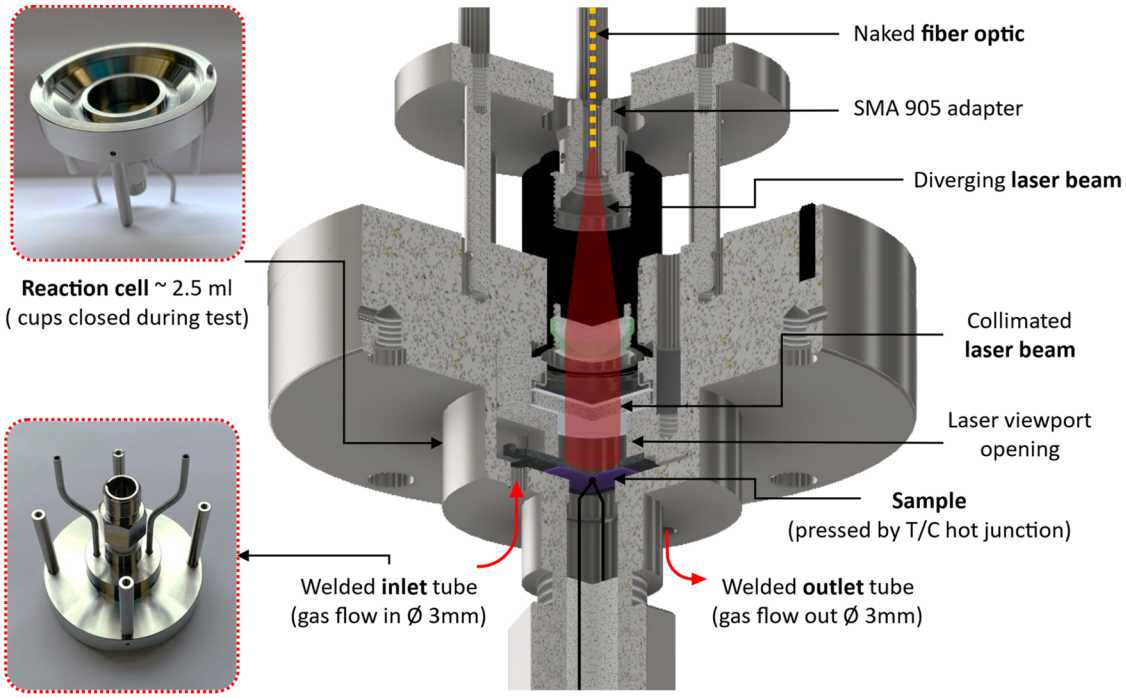

FIG. 3. 3D CAD model of the reaction cell showing the reaction cell closed during the test; an illustration of how the laser beam heats the sample from the backside and how the T/C measures the temperature of the active surface.

At the bottom of the lower cup, a vacuum-sealed NPT fitting (WFR series, Spectite Ltd.) passes the bare thermocouple leads (type K, Alumel/Chromel) through a Viton insulator. Figure 4 illustrates how the hot junction of the 0.1 mm diameter thermocouple wires is positioned to lightly press against the sample, ensuring sufficient physical contact for accurate temperature measurements. The opening of the sample holder and the spring plungers beneath the holder provide flexibility, allowing proper contact between the thermocouple and the sample. In this way, the exact temperature of the active surface of the model catalyst is measured. The thermocouple signal is transmitted directly to the proportional–integral–derivative (PID) controller (Eurotherm 3505 series) of the laser unit, which regulates the output power of the source.

3. Gas manifold and pumping system

The gas manifold consists of three gas lines: high-purity (N5) oxygen (O_2) and carbon monoxide (CO) as the primary reactants, and argon (Ar) as the carrier gas. Both reactant gases are connected to gas-specific, calibrated mass flow controllers (1179C Legacy series, MKS Instruments Inc.). To further purify the CO gas, a carbonyl trap (Leiden Probe Microscopy B.V.) is installed on the CO line before the MFC. The trap consists of copper tubing filled with pure Cu shots inside an insulated oven (heated to 300 °C during operation), followed by a cooling stage and a 15 μm particle filter downstream.

After passing through the MFCs, all three gases flow through check valves that allow unidirectional flow and prevent backflow or intermixing of the main gas lines. The gases are then combined in a single line and fed into the reaction cell through the gas inlet. The flow chart of the gas manifold is shown in Fig. 5. After each experiment, the gas lines and reactor are flushed with Ar and pumped to a pre-vacuum via bypass lines connecting the gas manifold to a scroll pump. The gas lines upstream of the MFCs are maintained at a pressure slightly above 1 bar to minimize contamination.

The vacuum in both the load-lock and the main chamber is maintained by turbomolecular pumps (80 l/s Pfeiffer HiPace 80) backed by a dry scroll pump (Leybold SC15). A UHV gate valve is installed between the main chamber and the rest of the pumping system to isolate the turbo pump during gas purging. This isolation allows the main chamber turbo pump to remain continuously operational, thereby avoiding time-consuming acceleration and deceleration. After the experiment, when the gas lines are shut off, pre-vacuum is achieved by opening the fore-pump valve to the scroll pump and then opening the gate valve connecting the running turbo pump, quickly establishing a vacuum. At this stage, the sample can be unloaded from the reaction cell and transferred or exchanged without venting or opening the UHV chamber.

The pressure-sensing system is illustrated in Figs. 5(a) and 5(b). Vacuum in the load-lock, main chamber, and gas inlet is monitored using vacuum gauges (Pirani/cold cathode, range 1×10^{-9} mbar to 1×10^{-1} mbar, Pfeiffer PKR360). Since the Pirani gauge is less precise at higher pressures (particularly for Ar), the absolute pressure in the main chamber (backfill pressure) is measured by a gas-insensitive capacitive manometer (INCONEL diaphragm, range 1×10^{-1} mbar to 10^{3} mbar, Leybold CERAVC CTR100). To monitor the vacuum level in the gas inlet when the gas lines are shut off

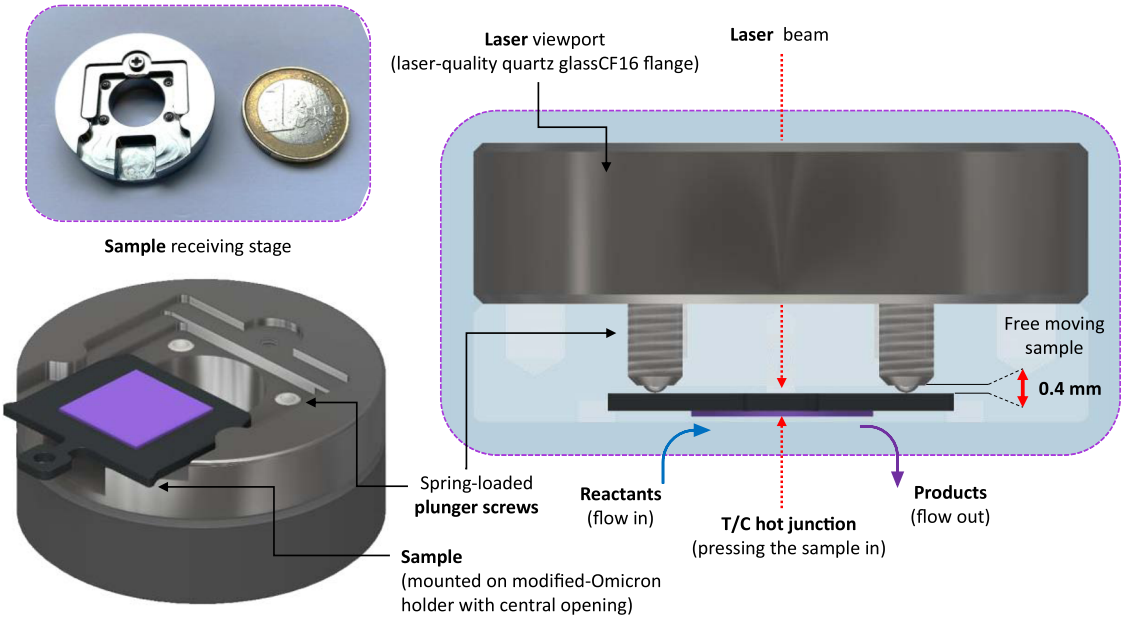

FIG. 4. Sample-receiving stage: physical contact between the T/C hot junction and the sample surface.

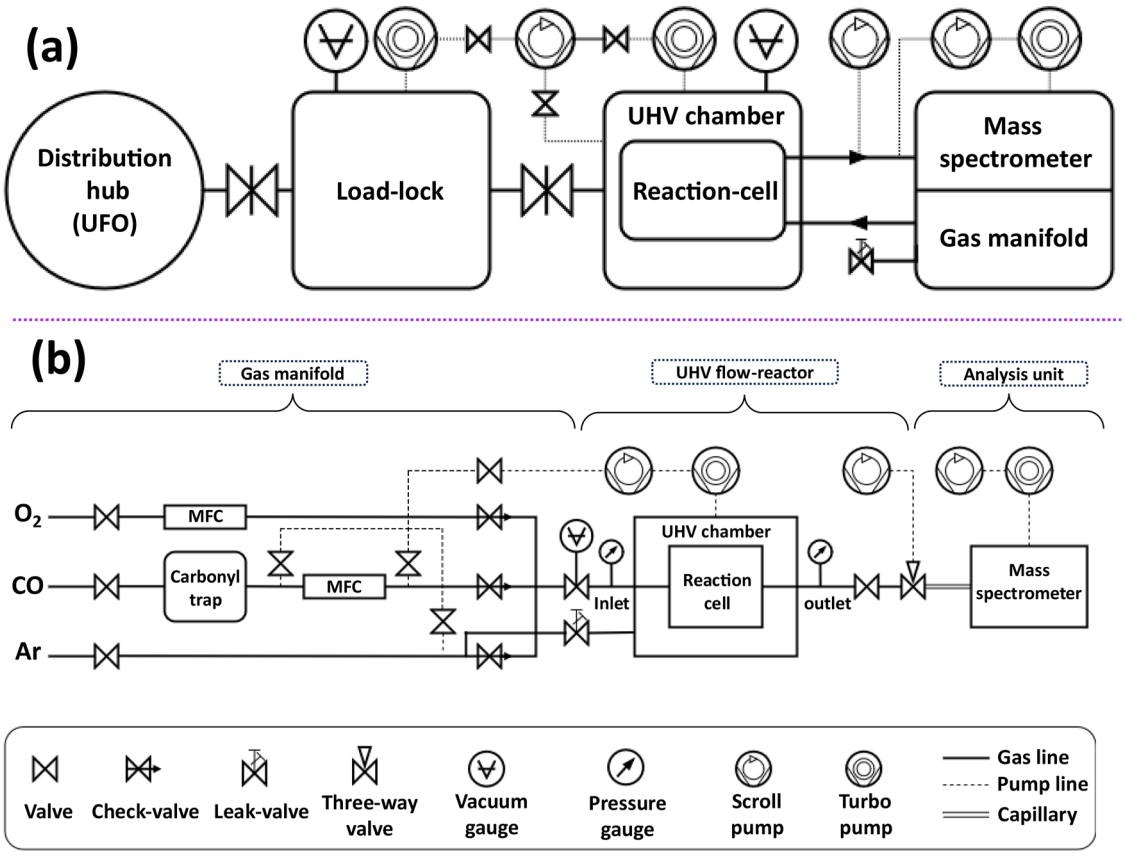

FIG. 5. (a) UHV schematic view of the CAT chamber pumping system; (b) detailed flow chart of the gas-handling unit, including the gas lines and the dosing system.

and pumped, a Pirani/cold cathode gauge (range 1×10^{-9} mbar to 10^{-1} mbar) measures the base vacuum. Absolute pressures in the inlet and reaction cell are measured by piezoresistive gauges (ceramic membrane, range 1 mbar to 2×10^{3} mbar, Leybold DU2000) installed on the gas tubes using Swagelok adapters, positioned immediately before and after the reaction cell. These gas-independent pressure gauges are suitable for measuring the absolute pressure of mixed gases and provide accurate pressure measurements within the reaction cell. The difference between the readings of the two sensors indicates any potential gas leak into or out of the reaction cell. The pumping system and pressure sensing in the gas analysis unit are described in the following section.

4. Gas analysis unit

A quadrupole mass spectrometer (QMS, HIDEN HPR-20 TMS) is employed to analyze the product gases. The QMS is equipped with a Pulse Ion Counting (PIC) secondary electron multiplier detector (<5 ppb detection limit) and a heated quartz-lined inlet capillary (QIC). During the entire experiment, the QMS records the mass intensities of five gases: O_2, CO, CO_2, H_2O, and Ar. Here, Ar serves as both an inert carrier gas and an internal reference to normalize the recorded intensities.

Gas concentrations are quantified using the QMS software (QGA 2.0), accounting for background signals in the zero scan, spectral overlap of mass peaks, and relative sensitivities. The processed data are ultimately reported as corrected partial pressures or percentages.

In Fig. 6, the detailed gas sampling method is illustrated. Gas exits the reaction cell, driven by differential pumping at the QMS inlet. A 1/8 in. Swagelok T-piece connects the 3 mm-diameter gas outlet tube to the diaphragm pump of the first pumping stage. A variable needle valve is installed here to control the pumping rate in the first stage according to the pressure in the reaction cell. On the other side, a tube fitting adapter connects the QIC tip (1/16 in. male Swagelok fitting) to the T-piece. The ultra-low-flow quartz capillary is fixed inside a sheathed flexible tube using a rubber ferrule. A resistive heating element is wrapped around the quartz capillary inside the protective tube, heating the inlet up to 200 °C to minimize gas and vapor condensation.

At the interface between the capillary and the QMS chamber, the second pumping stage is located. A second variable leak valve controls a bypass line to the QMS scroll pump, maintaining the pressure inside the QMS chamber below 5×10^{-6} mbar, which is within the safe operating range for the analyzer detector. This differential pumping configuration improves gas flow stability and enables precise control of the pressure inside the reaction cell.

III. OPERATION AND PERFORMANCE TEST OF THE REACTOR

In this section, a brief description of system operation and additional information about the calibration tests are presented. Prior to measurement with the CAT system, the model catalyst sample is prepared. The reference model samples (e.g., single crystals) are cleaned using special procedures and then loaded into the CAT load-lock for measurement. The cluster-assembled model catalysts with desired characteristics (i.e., support material, cluster size, areal coverage, deposition energy, etc.) are designed and subsequently

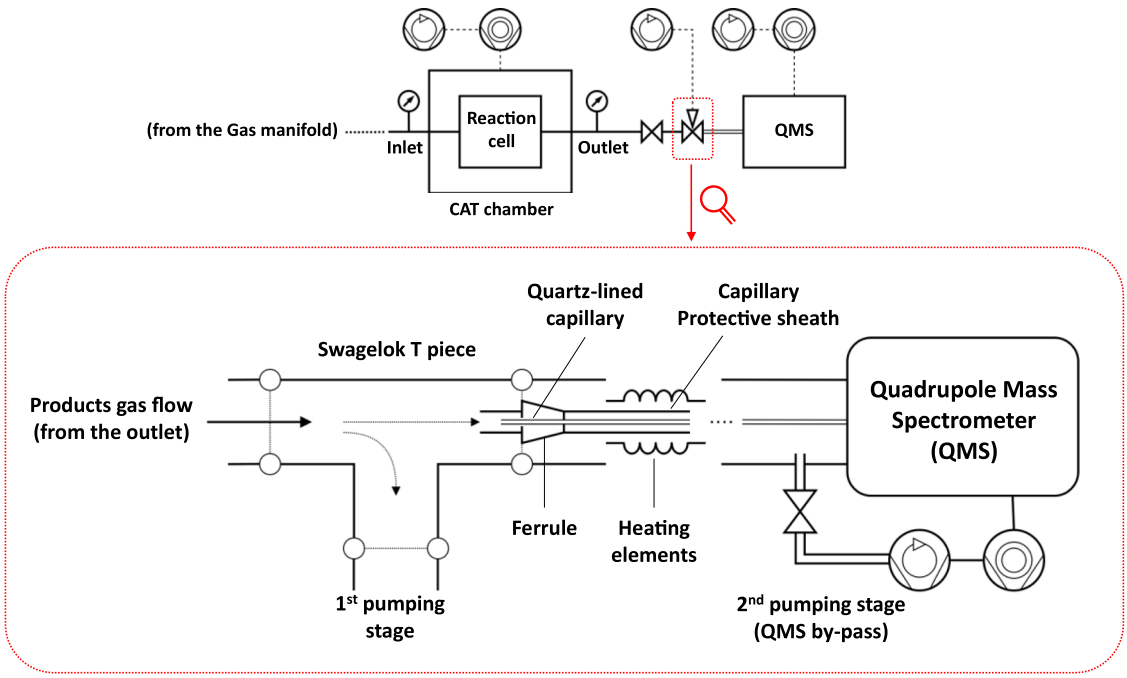

FIG. 6. Flowchart of the gas analysis unit: illustration of the gas sampling via QIC setup.

prepared. Prior to cluster deposition, the base substrate (typically a Si or Si/SiO_2 wafer) is cleaned using chemical solvents in an ultrasonic bath and then mounted on an Omicron sample holder. After transfer to the PLD load-lock, the oxide thin film is deposited with the desired thickness, crystal structure, and morphology. In the next step, the sample is transferred under UHV to the CIBD system, and the metal clusters with the desired size and coverage are deposited onto the oxide layer. During cluster deposition, the current of the charged clusters is monitored on the substrate using a picoamperemeter. Since the generated clusters carry a single negative charge (Pt_N^{-1}), the total deposited charge, and subsequently the total number of deposited clusters, can be determined from the measured current and deposition time. From this value, the cluster loading and corresponding areal coverage are calculated based on the total substrate area. Once the deposition current is calibrated with respect to time, target coverages, corresponding to defined

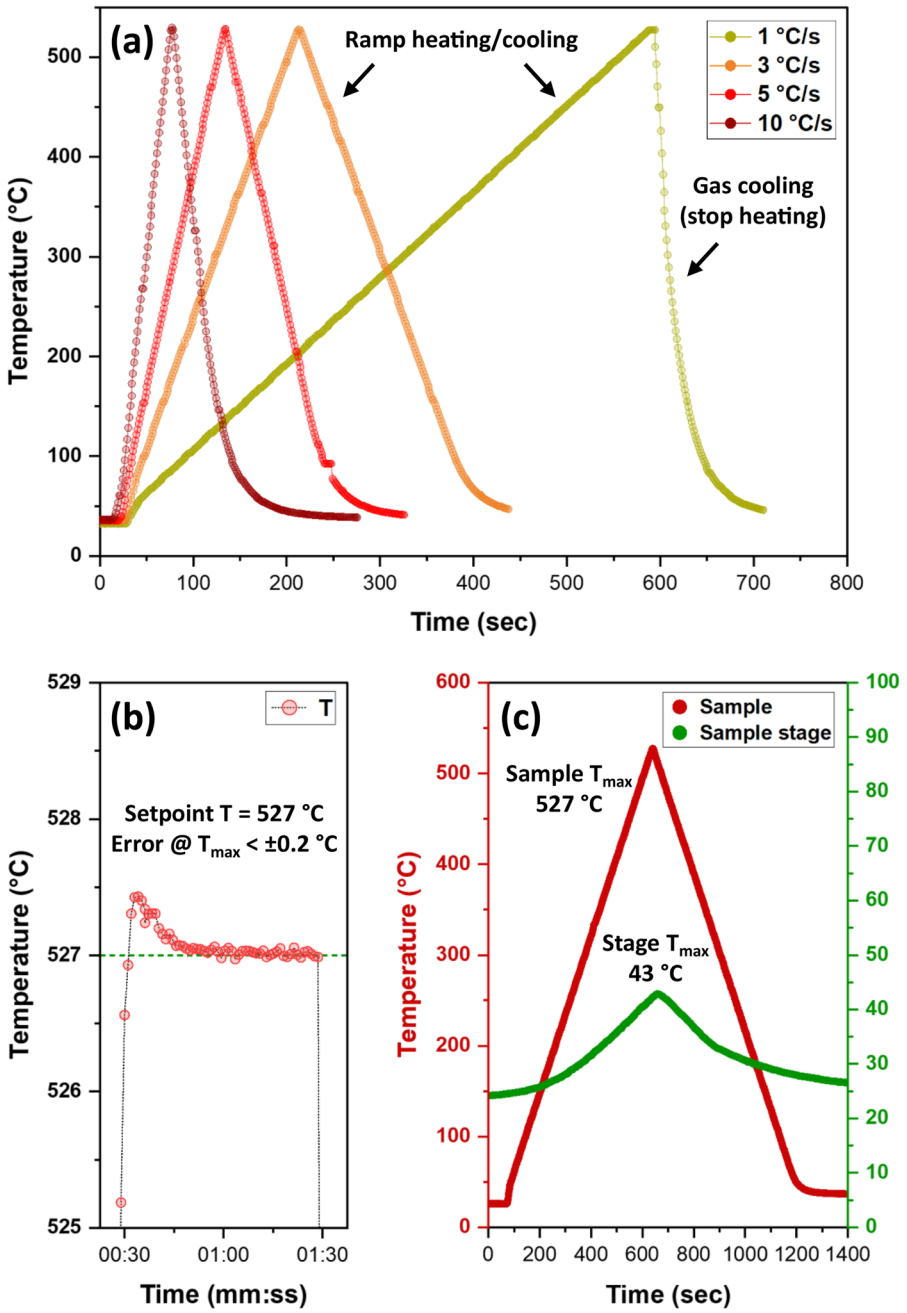

FIG. 7. Characterization of the heating unit performance: (a) temperature profile of the sample surface during the heating/cooling ramps (different rates) recorded vs time; (b) accuracy at set-point temperature via PID-controlled laser heater (<0.2 °C fluctuation at the setpoint); (c) heat leak from the hot sample to the sample stage.

cluster–cluster distances, can be precisely designed and reproducibly prepared.

Before catalytic testing, the sample is analyzed by XPS to determine the elemental composition of the oxide film and the metal clusters. The amount of active material can be estimated by comparison with previous reference samples.

Next, the sample is transferred from the CAT load-lock to the reaction cell under vacuum. By opening the main gate valve, the transfer arm accesses the sample and loads it onto the sample stage. At this point, the gate valve in front of the pumping line is opened, and the main chamber is pumped. With the reaction cell still open, the sample undergoes a cleaning routine to remove any residual species from the surface. This routine may include heating in vacuum and/or backfilling with argon.

After cleaning, the manipulator moves the upper cup down to close the cell, and the gas mixture is introduced into the reaction cell. The gas lines have already been flushed with Ar and pumped to pre-vacuum. After setting the desired ratio of reactant gases (stoichiometric, rich, or lean), the main inlet and outlet valves are opened. The leak valve is used to adjust the backfill gas pressure slightly above the cell pressure to establish isostatic conditions, minimizing gas leakage. The outlet gas flow, driven by the differential pumping system, reaches the tip of the heated capillary tube. The cell pressure (and consequently the QMS chamber pressure) can be further controlled by the first-stage pumping power. Once the QMS pressure is stabilized and a steady mass spectrometer signal is achieved, the heating program is initiated, and the gas analyzer records the masses of all gases (O_2, CO, CO_2, Ar, and H_2O) and temperature data as a function of time.

In Fig. 7, the calibration and performance tests of the CAT system are presented. Sample heating by the laser beam enabled precise and controllable programming of the temperature profile. As shown in Fig. 7(a), different heating and cooling ramps were employed, ranging from rapid (10 °C/s) to moderate (1 °C/s) rates, all of which closely followed the programmed profiles. It is worth noting that controlled cooling ramps utilize the balance between the laser heating and the flow of gas inside the reaction cell as the cooling medium. The gas flowing in the inlet tube is at room temperature and heats up as it flows over the hot sample. Therefore, the flow of cold gas over the sample's surface dissipates the thermal energy of the hot sample. The amount of heat uptake depends on the flow rate and pressure of the gas. Additional tests were performed at different cell pressures, which showed that the gas temperature can reach up to 50% of the sample temperature (see supplementary material, Fig. S1).

Figure 7(b) demonstrates the accuracy of the sample temperature at the setpoint. The heating unit achieved a setpoint of 527 °C with an accuracy of $<\pm 0.2$ °C and a short-time overshoot of less than 0.5 °C. Maintaining a stable temperature at the sample surface is crucial in flow reactors, as the overflowing (cold) gas continuously decreases the sample temperature. Therefore, careful consideration of the temperature sensor placement is essential. If the sensor is connected to the hot plate or the sample holder near the active surface, higher gas flows can induce significant discrepancies between the measured and actual temperature at the active surface. An accurate PID loop coupled with a well-positioned temperature sensor ensures the required precision.

The accuracy of the temperature measurement [reported in Fig. 7(b)] refers to the laser-focused spot (5 mm diameter). As previously mentioned, the collimating lens is designed to match the beam size to the deposited spot (5 mm diameter) of the active material. However, to ensure the uniformity of the lateral temperature distribution across the sample's surface, additional validation tests were conducted (see supplementary material, Figs. S2 and S3), which confirmed a uniform temperature distribution.

Figure 7(c) depicts the so-called heat leak from the hot sample to the sample-receiving stage, which is crucial for evaluating the localization of the heating method. Since the active material on model catalyst samples is very limited, heating of the surrounding parts can introduce background signals, potentially causing significant errors by generating reactions on unwanted surfaces. During the heat-leak test, two type-K thermocouple leads were attached to both the sample and the sample stage. Upon heating the sample at 1 °C/s to 527 °C (800 K), the stage temperature began increasing from $T_{sample} > 300$ °C and reached a maximum of 43 °C. This test confirmed the localized heating of the samples, demonstrating minimal thermal contact between the sample and the sample stage assembly, as well as precise alignment of the collimated laser beam.

Figures 8(a)–8(c) show the mass signals of O_2 (16 m/z), CO (28 m/z), CO_2 (44 m/z), and Ar (20 m/z) recorded during the zero scan (with a blank sample holder) and background scan (before/after the main test). The zero scan is performed to evaluate the performance of the gas analyzer and the sealing of the reaction cell. During the zero-scan, the main chamber is backfilled with Ar, while a typical reactant mixture (1% CO, 20% O_2 in Ar at 200 mbar) flows into the cell. The CO_2 signal recorded during the test on the Pt crystal (control sample) shows a clear CO/CO_2 evolution upon heating. During the light-on period, the decrease in the CO signal is more pronounced than that of O_2, reflecting the differences in concentrations and the excess O_2 in the reactant mixture. In addition, the slight increase in the Ar signal may be due to backfill Ar leaking into the cell. After cooling the sample, all signals return to their initial levels.

Figure 8(b) compares the CO_2 signals for the Pt single crystal with those of a blank sample holder during the same test. The stable CO_2 signal of the blank confirms that no reaction occurs on unwanted surfaces, even at high temperatures.

After completing the heating/cooling loop, the gas inlet was closed and the reaction cell was opened, allowing the mass spectrometer (MS) to sample the backfill gas in the main chamber. Figure 8(a) shows that, upon closure of the inlet, the reactant gas signals drop immediately. Signals recorded after opening the cell match those from the background scan [Fig. 8(c)] performed before the test (backfilled Ar). This observation indicates that the slightly higher backfill pressure in the main chamber compared to the cell pressure effectively minimizes diffusion of reactant gases from the cell, confirming the integrity of the sealing method. Consequently, the calculation of species concentrations is accurate and reliable.

In the following section, catalytic CO oxidation is studied as a proof of concept on two model systems [Pt(110) and oxide-supported Pt clusters]. The acquired data are compared with literature values to validate the performance of the new reactor.

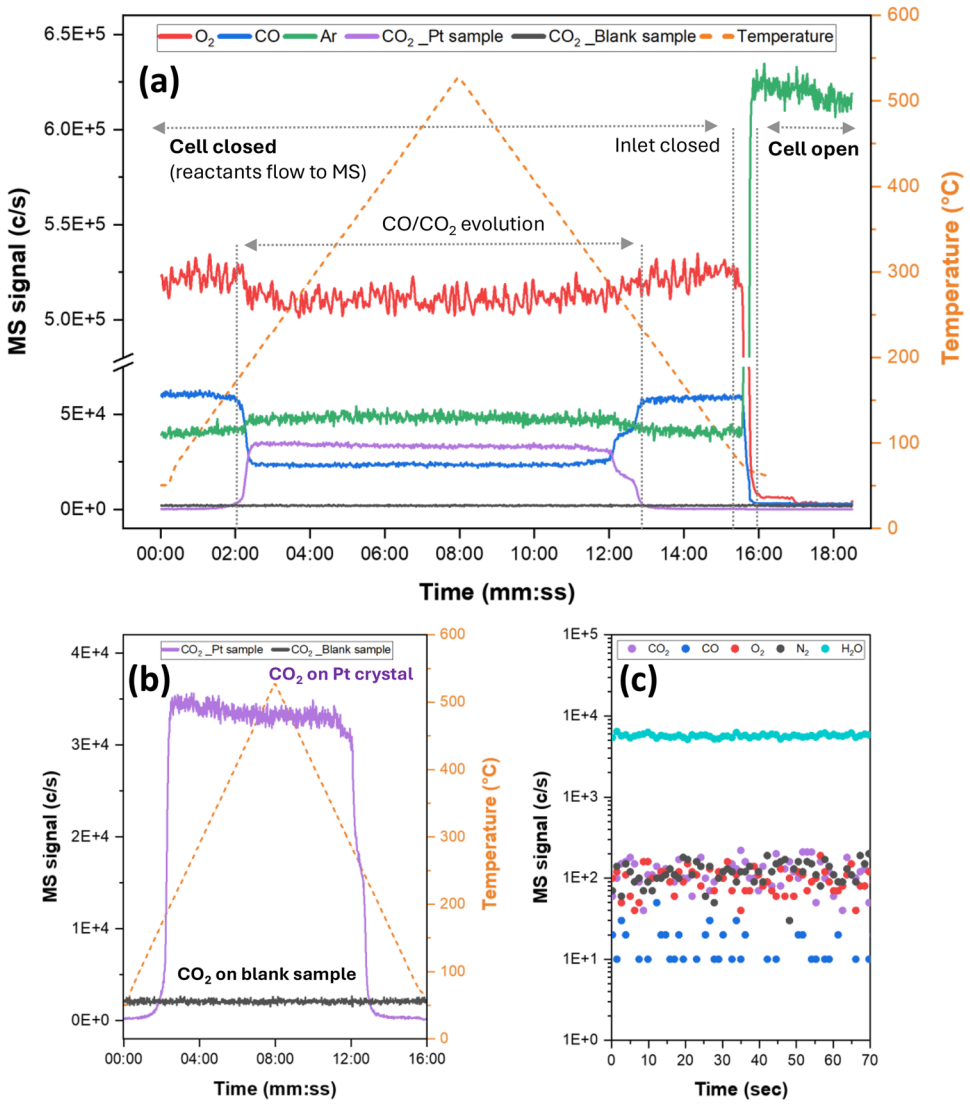

FIG. 8. QMS mass signals recorded vs time showing: (a) CO/CO_2 evolution on a blank sample vs Pt single crystal; the stable flow of gases during the zero-scan and no reactant diffusion out of the cell; (b) zoom-in view of the zero scan on the blank sample compared with the Pt single crystal; (c) background gas signals recorded before/after the main scan (H_2O signal corresponds to the remaining amount in the QMS chamber).

IV. RESULTS AND DISCUSSION

A. CO oxidation on Pt (110) single crystal

Pt(110) is a well-studied model catalyst due to its anisotropic atomic structure, which includes both terrace and step sites within the same crystallographic plane.[30–32] This structural complexity allows for the probing of site-specific reaction pathways and surface reconstructions under reaction conditions. Compared to the most reactive and close-packed Pt(111) surface, which often maintains structural stability under reaction conditions, Pt(110) is prone to reorganization under CO/O_2 adsorption and exhibits more complex surface behavior, including reconstruction and bistability during CO oxidation. In early work, Ertl and coworkers studied the surface reconstruction and oscillations of CO oxidation on Pt(110) to model its bistable behavior.[30]

In this work, the Pt(110) crystal surface was first treated by cyclic Ar^+ sputtering and UHV annealing to ensure a well-defined model surface prior to testing. The crystal (6 mm diameter) was held on a modified Omicron holder via the central groove and subjected to repeated cycles of Ar^+ sputtering (1.5 keV in an Ar pressure of 3×10^{-6} mbar at RT), followed by annealing at 550 °C between sputtering cycles. This procedure removed ~250 monolayers from the surface. Catalytic tests were conducted under 200 mbar cell pressure, with temperatures ranging from RT to 527 °C (800 K), and at varying CO concentrations. Between test cycles, the sample surface was heated in Ar at elevated temperature to remove any residual species.

The results of reactive CO oxidation on the Pt(110) surface are illustrated in Figs. 9(a)–9(c). The light-off temperature exhibits a substantial shift (150–350 °C) as the CO content increases [Fig. 9(a)], suggesting that CO poisoning or high CO adsorbate

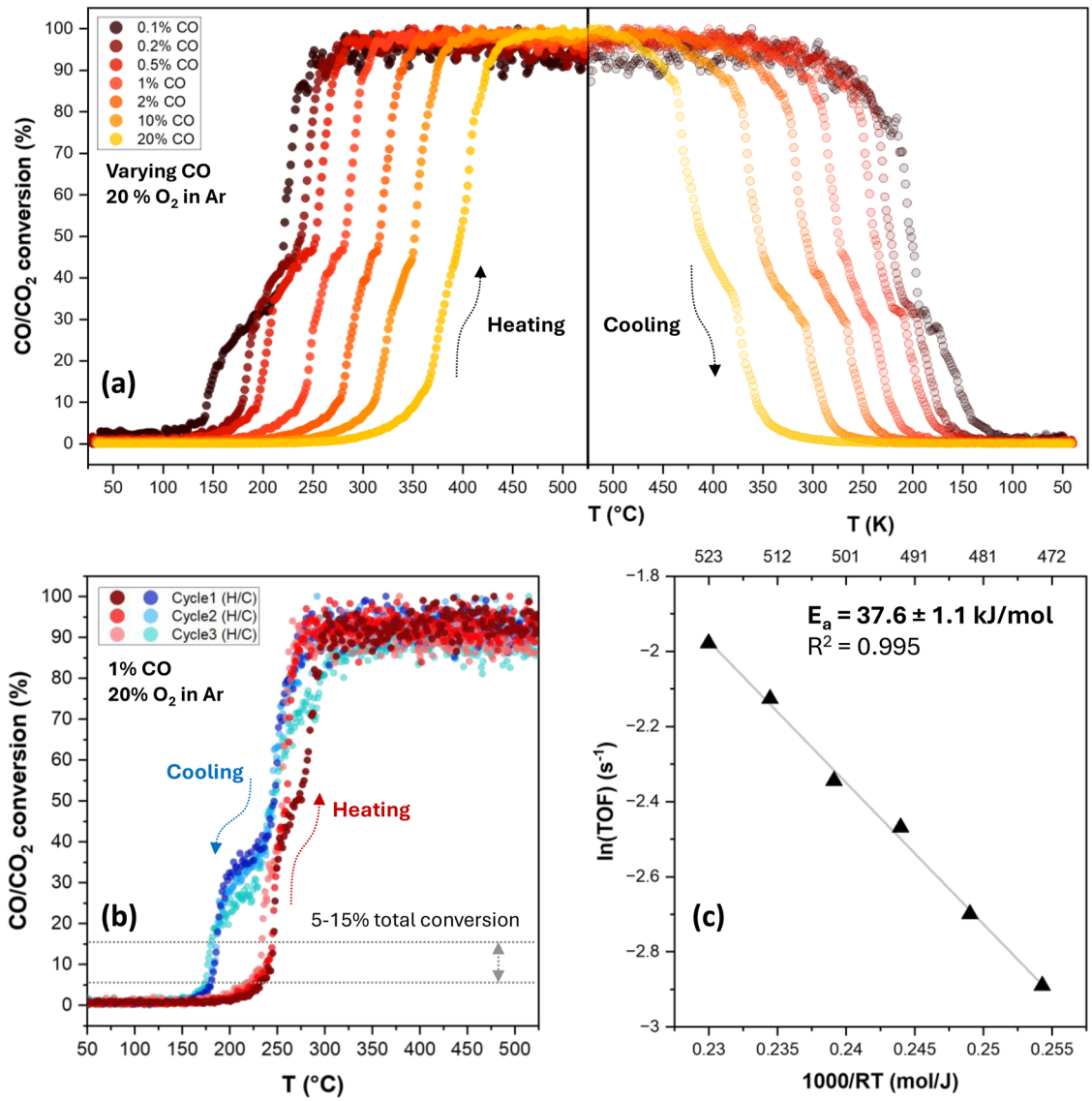

FIG. 9. CO oxidation on Pt (110) single crystal surface at 200 mbar: (a) reactive heating/cooling at 50–527 °C (O_2 20% constant, rest Ar) shows the hindrance of CO/CO_2 conversion with increasing CO content; (b) three cycles of heating/cooling at 1% CO (20% O_2 in Ar) showing the hysteresis; (c) Arrhenius plot of the turnover frequency (TOF) for CO/CO_2 conversion on Pt (110). [Note: for the calculation of TOF, see below in the text].

coverage suppresses catalytic turnover until sufficient thermal energy is available to desorb or react adsorbed CO. This behavior is consistent with competitive adsorption: CO has a higher adsorption probability, blocks active sites, and suppresses O_2 adsorption or dissociation.[31]

For further study and comparison, a 1% CO mixture was chosen. Figure 9(b) displays consecutive heating/cooling cycles conducted at 1 °C/s. The light-off and light-out curves display symmetrical heating/cooling behavior with a wide hysteresis loop. During heating, the CO_2 onset temperature is delayed, while during cooling, the reaction persists to lower temperatures than expected from a simple reversible mechanism. Such hysteresis is well known for CO oxidation on Pt(110) and is attributed to surface structural changes (e.g., reconstructions between the 1 × 1 and 1 × 2 phases), differential adsorption energies, and possibly the formation of subsurface oxygen or an oxide layer.[30,31]

In all tests on Pt(110), a distinct "kink" is observed during both heating and cooling. The reaction rate increases sharply at the kink temperature rather than gradually, indicating that more than one type of active site (exposed terraces and edges) becomes operative, or that a phase transition occurs in the surface structure. This observation aligns with previous studies of reaction-induced reconstruction

on Pt(110), which leads to varied diffusion, adsorption, and reaction rates along different crystal directions.[20,30,33,34]

To evaluate the reaction rate and activation energy, the low-temperature region (5%–15% total conversion, where most active sites are assumed to be operative) was analyzed. The experimentally determined temperature uncertainty in the low-temperature region was minimal, and its potential contribution to the overall uncertainty is expected to be negligible. The turnover frequency (TOF) was determined from the CO_2 production rate, calculated based on the measured partial pressures and gas flow, and normalized to the number of surface Pt atoms on the crystal. The surface atom count was estimated from the geometric surface area of the Pt(110) crystal and the known surface atomic density corresponding to the Pt(110) facet, assuming full surface exposure of active sites [Fig. 9(c)]. Applying the Arrhenius equation, the apparent activation energy (E_a) of 37.6 ± 1.1 kJ/mol was obtained for the Pt(110) surface, in good agreement with literature values for a similar system.[30,33,35,36]

B. CO oxidation on oxide-supported Pt clusters

Supported noble metal clusters—particularly monodispersed systems—serve as excellent model catalysts due to their tunable size, defined structure, and strong metal–support interactions.[4,37–42] As a model catalyst, Pt_N/CeO_2 (N = 200 atoms) was prepared to evaluate the performance of the CAT system in the measurement of delicate samples. In contrast to single-crystal surfaces, which provide a high number of active sites, ceria-supported mass-selected clusters with low areal coverage offer a very limited number of active sites. Therefore, highly accurate and reliable measurement techniques are required to study such delicate systems.

CeO_2 redox flexibility provides lattice oxygen to the active sites and stabilizes small Pt clusters through strong metal–support interactions.[43–46] Therefore, a CeO_2 thin film was deposited using PLD on a silicon wafer as the oxide support for the Pt clusters. The deposition of CeO_2 was performed at a substrate temperature of 550 °C and an O_2 partial pressure of 0.05 mbar, resulting in a continuous film with 15 nm thickness. The sample was subsequently

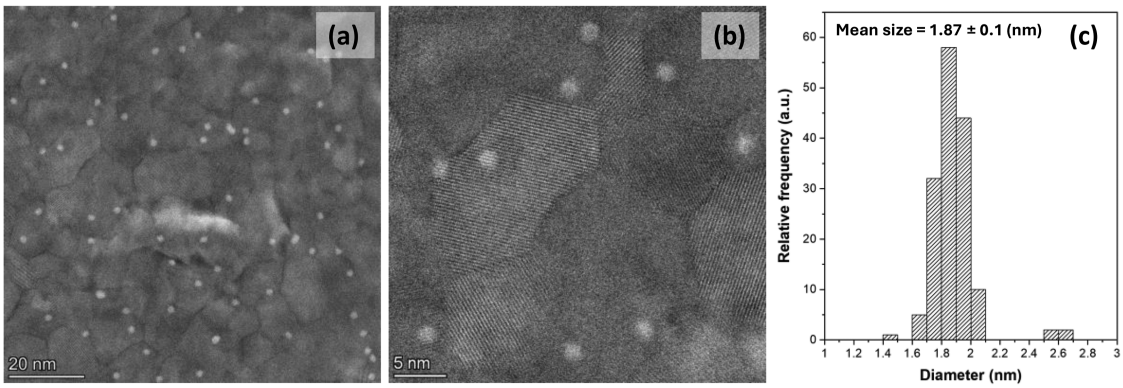

FIG. 10. [(a) and (b)] STEM images of Pt_{200} clusters deposited on a CeO_2 thin film; (c) the narrow size distribution of Pt_{200} clusters, confirming the precision of the mass-selection method.

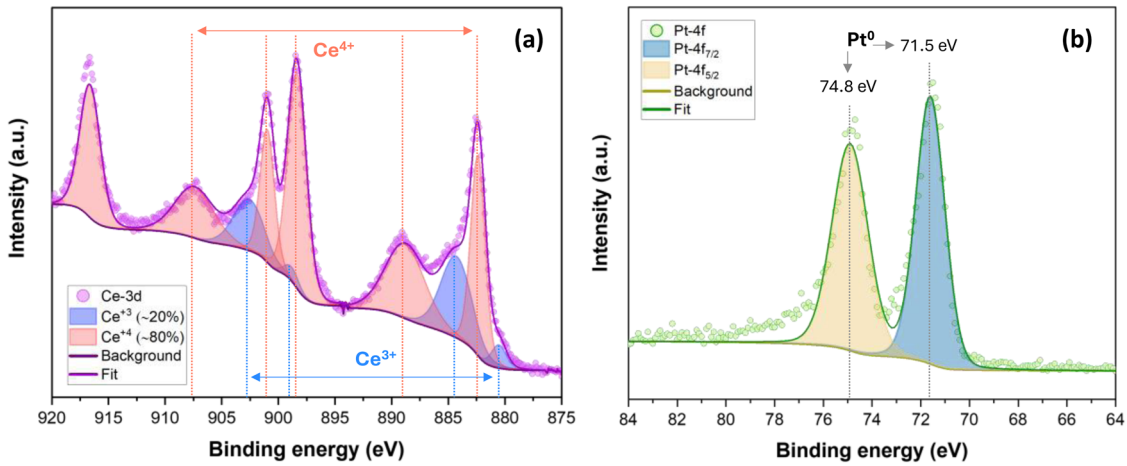

FIG. 11. XPS surface analysis of the Pt_{200}/CeO_2 catalyst: (a) Ce 3d region scan shows Ce^{4+}/Ce^{3+} multivalency of 80%–20%; (b) Pt 4f region scan demonstrates a dominant Pt^0 doublet peak, confirming metallic Pt clusters.

transferred to the CIBD system, where Pt_{200} clusters (1.9 nm diameter) were deposited on the CeO_2 thin film under soft-landing conditions (<0.1 eV per Pt atom) to achieve an areal coverage of 5%. A low coverage was intentionally chosen to minimize sintering during catalytic operation and to assess the detection sensitivity of the CAT system. The STEM images shown in Figs. 11(a) and 11(b) depict the homogeneous spatial distribution of Pt_{200} clusters on the oxide support. Moreover, Fig. 10(c) presents the size distribution analysis of the corresponding Pt_{200} clusters with a mean size of 1.87 nm. The well-defined size range demonstrates the successful preparation of dispersed clusters with minimal agglomeration.

Prior to catalytic testing, the elemental composition of the deposited clusters and the oxide support was analyzed by XPS at RT at 5×10^{-9} mbar, using an Al Kα source (1486 eV). The spectra were analyzed and deconvoluted using CasaXPS software. As shown in Fig. 11(a), the Ce 3d orbital photoemission peaks appear in the binding energy range of 880–920 eV. In cerium oxide, Ce often exhibits both Ce^{3+} and Ce^{4+} oxidation states, and XPS is

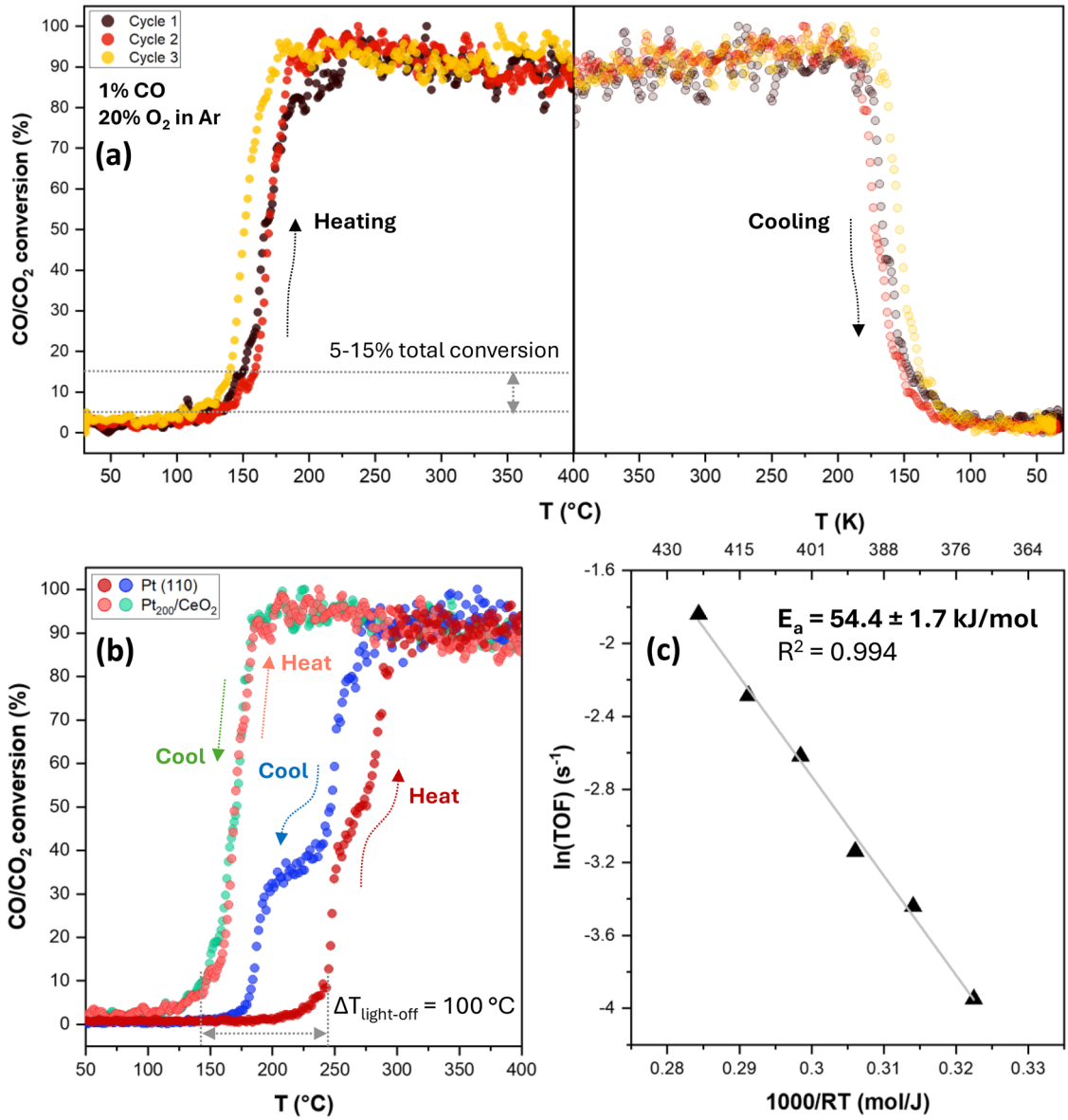

FIG. 12. CO oxidation on Pt_{200}/CeO_2 at 200 mbar: (a) cyclic reactive heating/cooling at 50–400 °C (1% CO, 20% O_2 in Ar) displays no significant hysteresis; (b) comparison of light-on/out curves of Pt_{200}/CeO_2 with the Pt (110) surface at 1% CO (20% O_2 in Ar); (c) Arrhenius fit of TOF values showing the activation energy for CO/CO_2 conversion on supported Pt_{200} clusters.

extensively employed to investigate these valence states.[47] Deconvolution of the XPS data, using established fitting parameters for Ce^{3+} and Ce^{4+} from the literature,[48,49] indicates multivalency with a Ce^{4+}/Ce^{3+} ratio of ~80%–20%. The mixed-valence composition suggests the presence of oxygen vacancies (O_v) in the deposited film.

The analysis of the Pt 4f spin–orbit doublet ($4f_{7/2}$–$4f_{5/2}$) shows a doublet separation of 3.3 eV, a peak area ratio ($4f_{7/2}$:$4f_{5/2}$) of 4:3, and binding energies of 71.5 and 74.8 eV for $4f_{7/2}$ and $4f_{5/2}$, respectively [Fig. 11(b)]. These parameters confirm that the clusters remain in the metallic state (Pt^0) with no oxidation during deposition and are in excellent agreement with previously reported literature.[24,43]

To compare the reactivity of the oxide-supported Pt_{200} clusters with Pt(110), three consecutive cycles of catalytic oxidation of CO were carried out under similar conditions (temperature range from RT to 400 °C and 200 mbar total cell pressure), and the results are shown in Figs. 12(a) and 12(b). The CO_2 production of CeO_2-supported Pt_{200} clusters ignites at lower temperatures (126 °C) under similar reaction conditions (200 mbar, 1% CO, and 20% O_2 in Ar). This suggests that the clusters provide a higher density of active sites and that the CeO_2 support contributes to the oxygen supply. The potential pathway for the contribution of the oxide support can be via mobile oxygen vacancies, thereby lowering the barrier for CO oxidation. CeO_2 is known for its high oxygen storage capacity and facile redox cycling between Ce^{3+} and Ce^{4+}, which can supply surface oxygen during the reaction and sustain catalytic activity. These synergistic effects likely contribute to the superior catalytic performance and stability observed for the Pt_{200}/CeO_2 system.[44,45,50–53]

As shown in Fig. 12(a), after the first cycle of CO oxidation, the light-off temperature for the CeO_2-supported Pt_{200} clusters exhibits a slight decrease, while the total conversion remains stable over three consecutive cycles. This cyclic stability demonstrates that the Pt_{200}/CeO_2 catalyst maintains catalytic activity and resists deactivation over multiple light-off cycles, particularly when cluster sintering is minimized and strong metal–support interactions are preserved.

To evaluate the reaction rate of the supported Pt_{200} clusters, the low-temperature region (5%–15% total conversion) with minimal temperature uncertainty was analyzed. Based on the known cluster size (Pt_N, N = 200 atoms), the areal coverage, and the deposited surface area, the total number of Pt atoms on the CeO_2 thin film was estimated. The number of surface and interfacial Pt atoms contributing to the reaction was determined using a geometric model (developed by Cargnello *et al.*[53]). Using the measured CO_2 formation rate derived from the partial pressures, the TOF in the low-temperature region was then calculated. The Arrhenius plot fits the calculated TOF values well [Fig. 12(c)], yielding an apparent activation energy (E_a) of 54.4 ± 1.7 kJ/mol, which is consistent with literature reports for supported clusters/nanoparticles smaller than 2 nm. The agreement between the measured data and previously reported results, along with reproducibility, confirms the reliability and precision of the newly designed UHV reactor for studying various model catalysts.[7,43,44,46,53–58]

The cyclic heating/cooling hysteresis of the supported clusters is insignificant compared to that of Pt(110), suggesting rapid reversibility of adsorption/desorption dynamics, quick equilibration, and reduced competitive adsorption of CO and O_2. In contrast to Pt(110), where low-temperature CO adsorption blocks active sites and hinders the reaction, Pt_{200}/CeO_2 exhibits a smooth transition from low to high reactivity (Fig. 13). This gradual increase is consistent with the operation of the Mars–van Krevelen mechanism at the cluster–support interface, where the participation of lattice oxygen reduces surface competition.[7,44,45,51–53,58] The support contribution eliminates the need for an additional O_2 adsorption step, as required on the Pt single crystal, leading to an earlier reaction onset and a smooth transition between the low- and high-reactivity regimes

Moreover, the absence of the "kink" in the light-off curve for the supported clusters indicates greater uniformity in active site behavior. Unlike the abrupt transitions observed on Pt(110), the onset of CO oxidation on clusters is smoother, suggesting that catalytic sites across the cluster population and support interface

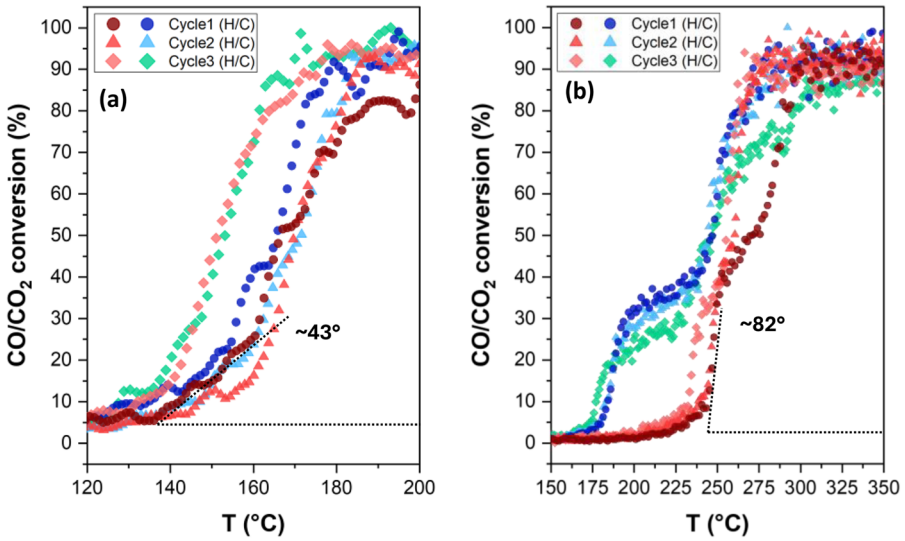

FIG. 13. Zoomed-in view at the light-off region of (a) Pt_{200}/CeO_2 and (b) Pt(110) surface. The gradual initial slope of supported Pt clusters indicates less surface competition and oxygen supply from the oxide support.

are more similar, or that structural or phase changes are less pronounced. Literature reports support that smaller particles or clusters often exhibit less distinct structural transitions and more distributed reactivity.[7,45,53]

V. CONCLUSION

A novel UHV-compatible flow reactor with a small volume (2.5 mL) was developed to enable precise testing of model catalysts under well-controlled conditions. The two-cup design of the reaction cell, combined with the differential-pressure sealing method, allowed for high sensitivity in product detection. Localized heating via a PID-controlled NIR laser provided accurate control over the sample temperature, while the integration of the reactor into the UHV facility ensured that the sample remained contaminant-free throughout the entire experimental workflow, preserving surface cleanliness and enabling reproducible measurements.

The reactor's functionality was validated through CO oxidation studies on two model catalysts: a Pt(110) single crystal and CeO_2-supported mass-selected Pt_{200} clusters. The Pt(110) system exhibited the expected hysteresis behavior, light-off temperature shifts, and surface restructuring effects. In contrast, Pt_{200}/CeO_2 clusters demonstrated a lower light-off temperature, smooth reactivity onset, enhanced cyclic stability, and no hysteresis, reflecting the critical role of oxide support in facilitating oxygen activation. The calculated activation energies align with literature values, confirming the accuracy and reliability of the system.

With the functionality of the new reactor now established, its application can be extended to the investigation of a broader range of heterogeneous catalytic reactions, including CH_4 activation, NH_3 oxidation, and NO_x reduction. Furthermore, integration with the CIBD technique opens new possibilities for precise fabrication of cluster-assembled model catalysts, while the reactor's modular design provides a robust and accurate testing environment. This combination offers a versatile platform for systematic investigations across catalytic materials and reaction conditions, bridging the gap between fundamental surface science and realistic catalytic environments.

SUPPLEMENTARY MATERIAL

Additional calibration and validation tests related to temperature measurement are provided in the supplementary material, and the corresponding data are available online.

ACKNOWLEDGMENTS

This study was funded by the Deutsche Forschungsgemeinschaft (DFG, German Research Foundation) within the framework of the Collaborative Research Center—TrackAct (SFB 1441: Project ID No. 426888090). The authors gratefully acknowledge the KIT Central Mechanical Workshop (Haustechnik) for its expert support in the design and fabrication of custom components. H.H. and R. S. sincerely thank Jan-Dierk Grunwaldt and Florian Maurer for their helpful discussions on the interpretation of the results. R. S. further expresses gratitude to Gleb Iankevich for valuable assistance and contributions in the initial operation of the CIBD system.

AUTHOR DECLARATIONS

Conflict of Interest

The authors have no conflicts to disclose.

Author Contributions

Ramin Shadkam: Conceptualization (lead); Data curation (lead); Formal analysis (lead); Methodology (lead); Writing – original draft (lead); Writing – review & editing (equal). **Martin Limbach**: Conceptualization (equal); Methodology (equal). **Mohana V. Kante**: Data curation (equal); Formal analysis (equal); Writing – review & editing (equal). **Ajai R. L. Nilayam**: Formal analysis (equal). **Christian Kübel**: Funding acquisition (equal); Project administration (equal); Writing – review & editing (equal). **Robert Kruk**: Conceptualization (equal); Project administration (equal); Supervision (equal); Writing – review & editing (equal). **Horst Hahn**: Conceptualization (equal); Funding acquisition (lead); Project administration (lead); Supervision (lead); Writing – review & editing (equal).

DATA AVAILABILITY

The data that support the findings of this study are available from the corresponding author upon reasonable request.

REFERENCES

[1] J. Gustafson, R. Westerström, A. Mikkelsen, X. Torrelles, O. Balmes, N. Bovet, J. N. Andersen, C. J. Baddeley, and E. Lundgren, "Sensitivity of catalysis to surface structure: The example of CO oxidation on Rh under realistic conditions," Phys. Rev. B **78**(4), 045423 (2008).
[2] C. Feng, X. Liu, T. Zhu, and M. Tian, "Catalytic oxidation of CO on noble metal-based catalysts," Environ. Sci. Pollut. Res. **28**(20), 24847–24871 (2021).
[3] H.-J. Freund and G. Pacchioni, "Oxide ultra-thin films on metals: New materials for the design of supported metal catalysts," Chem. Soc. Rev. **37**(10), 2224 (2008).
[4] U. Heiz, F. Vanolli, L. Trento, and W.-D. Schneider, "Chemical reactivity of size-selected supported clusters: An experimental setup," Rev. Sci. Instrum. **68**(5), 1986–1994 (1997).
[5] S. M. F. Shahed, A. Beniya, H. Hirata, and Y. Watanabe, "Morphology of size-selected Pt *n* clusters on CeO_2(111)," J. Chem. Phys. **148**(11), 114702 (2018).
[6] G. Rupprechter, "Operando surface spectroscopy and microscopy during catalytic reactions: From clusters via nanoparticles to meso-scale aggregates," Small **17**(27), 2004289 (2021).
[7] A. M. Gänzler, M. Casapu, D. E. Doronkin, F. Maurer, P. Lott, P. Glatzel, M. Votsmeier, O. Deutschmann, and J.-D. Grunwaldt, "Unravelling the different reaction pathways for low temperature CO oxidation on Pt/CeO_2 and Pt/Al_2O_3 by spatially resolved structure–activity correlations," J. Phys. Chem. Lett. **10**(24), 7698–7705 (2019).
[8] L. Mayr, R. Rameshan, B. Klötzer, S. Penner, and C. Rameshan, "Combined UHV/high-pressure catalysis setup for depth-resolved near-surface spectroscopic characterization and catalytic testing of model catalysts," Rev. Sci. Instrum. **85**(5), 055104 (2014).
[9] G. A. Somorjai and J. Y. Park, "Molecular surface chemistry by metal single crystals and nanoparticles from vacuum to high pressure," Chem. Soc. Rev. **37**(10), 2155 (2008).
[10] F. Gao, Y. Cai, K. K. Gath, Y. Wang, M. S. Chen, Q. L. Guo, and D. W. Goodman, "CO oxidation on Pt-Group metals from ultrahigh vacuum to near atmospheric pressures. 1. Rhodium," J. Phys. Chem. C **113**(1), 182–192 (2009).
[11] M. Roiaz, V. Pramhaas, X. Li, C. Rameshan, and G. Rupprechter, "Atmospheric pressure reaction cell for operando sum frequency generation spectroscopy of ultrahigh vacuum grown model catalysts," Rev. Sci. Instrum. **89**(4), 045104 (2018).

[12]F. Gao, Y. Wang, Y. Cai, and D. W. Goodman, "CO oxidation on Pt-Group metals from ultrahigh vacuum to near atmospheric pressures. 2. Palladium and platinum," J. Phys. Chem. C **113**(1), 174–181 (2009).
[13]M. Johansson, J. Hoffmann Jørgensen, and I. Chorkendorff, "Combined high-pressure cell–ultrahigh vacuum system for fast testing of model metal alloy catalysts using scanning mass spectrometry," Rev. Sci. Instrum. **75**(6), 2082–2093 (2004).
[14]Y. Watanabe and N. Isomura, "A new experimental setup for high-pressure catalytic activity measurements on surface deposited mass-selected Pt clusters," J. Vac. Sci. Technol., A **27**(5), 1153–1158 (2009).
[15]S. Blomberg, U. Hejral, M. Shipilin, S. Albertin, H. Karlsson, C. Hulteberg, P. Lömker, C. Goodwin, D. Degerman, J. Gustafson, C. Schlueter, A. Nilsson, E. Lundgren, and P. Amann, "Bridging the pressure gap in CO oxidation," ACS Catal. **11**(15), 9128–9135 (2021).
[16]L. Caulfield, E. Sauter, H. Idriss, Y. Wang, and C. Wöll, "Bridging the pressure and materials gap in heterogeneous catalysis: A combined UHV, in situ, and operando study using infrared spectroscopy," J. Phys. Chem. C **127**(29), 14023–14029 (2023).
[17]H. J. Freund, G. Meijer, M. Scheffler, R. Schlögl, and M. Wolf, "CO oxidation as a prototypical reaction for heterogeneous processes," Angew. Chem., Int. Ed. **50**(43), 10064–10094 (2011).
[18]W. Chen, J. Cao, J. Yang, Y. Cao, H. Zhang, Z. Jiang, J. Zhang, G. Qian, X. Zhou, D. Chen, W. Yuan, and X. Duan, "Molecular-level insights into the electronic effects in platinum-catalyzed carbon monoxide oxidation," Nat. Commun. **12**(1), 6888 (2021).
[19]B. L. M. Hendriksen, S. C. Bobaru, and J. W. M. Frenken, "Looking at heterogeneous catalysis at atmospheric pressure using tunnel vision," Top. Catal. **36**(1–4), 43–54 (2005).
[20]M. A. van Spronsen, J. W. M. Frenken, and I. M. N. Groot, "Surface science under reaction conditions: CO oxidation on Pt and Pd model catalysts," Chem. Soc. Rev. **46**(14), 4347–4374 (2017).
[21]D. W. Blakely, E. I. Kozak, B. A. Sexton, and G. A. Somorjai, "New instrumentation and techniques to monitor chemical surface reactions on single crystals over a wide pressure range (10−8–105 Torr) in the same apparatus," J. Vac. Sci. Technol. **13**(5), 1091–1096 (1976).
[22]A. L. Cabrera, N. D. Spencer, E. Kozak, P. W. Davies, and G. A. Somorjai, "Improved instrumentation to carry out surface analysis and to monitor chemical surface reactions *in situ* on small area catalysts over a wide pressure range (10−8–105 Torr)," Rev. Sci. Instrum. **53**(12), 1888–1893 (1982).
[23]T. R. Henriksen, J. L. Olsen, P. Vesborg, I. Chorkendorff, and O. Hansen, "Highly sensitive silicon microreactor for catalyst testing," Rev. Sci. Instrum. **80**(12), 124101 (2009).
[24]T. Haunold, C. Rameshan, A. V. Bukhtiyarov, and G. Rupprechter, "An ultrahigh vacuum-compatible reaction cell for model catalysis under atmospheric pressure flow conditions," Rev. Sci. Instrum. **91**(12), 125101 (2020).
[25]F. Morfin and L. Piccolo, "A versatile elevated-pressure reactor combined with an ultrahigh vacuum surface setup for efficient testing of model and powder catalysts under clean gas-phase conditions," Rev. Sci. Instrum. **84**(9), 094101 (2013).
[26]S. Bonanni, K. Aït-Mansour, M. Hugentobler, H. Brune, and W. Harbich, "An experimental setup combining a highly sensitive detector for reaction products with a mass-selected cluster source and a low-temperature STM for advanced nanocatalysis measurements," Eur. Phys. J. D **63**(2), 241–249 (2011).
[27]K. Zhang, L. H. Wandall, J. Vernieres, J. Kibsgaard, and I. Chorkendorff, "Ultrahigh vacuum compatible reactor for model catalyst study of ammonia synthesis at ambient pressure," Rev. Sci. Instrum. **94**(11), 114102 (2023).
[28]A. Fischer, R. Kruk, and H. Hahn, "A versatile apparatus for the fine-tuned synthesis of cluster-based materials," Rev. Sci. Instrum. **86**(2), 023304 (2015).
[29]C. Benel, T. Reisinger, R. Kruk, and H. Hahn, "Cluster-assembled nanocomposites: Functional properties by design," Adv. Mater. **31**(26), 1806634 (2019).
[30]M. Eiswirth and G. Ertl, "Kinetic oscillations in the catalytic CO oxidation on a Pt(110) surface," Surf. Sci. **177**(1), 90–100 (1986).
[31]B. L. M. Hendriksen and J. W. M. Frenken, "CO oxidation on Pt(110): Scanning tunneling microscopy inside a high-pressure flow reactor," Phys. Rev. Lett. **89**(4), 046101 (2002).
[32]C. Ellinger, A. Stierle, I. K. Robinson, A. Nefedov, and H. Dosch, "Atmospheric pressure oxidation of Pt(111)," J. Phys. Condens. Matter **20**(18), 184013 (2008).
[33]A. von Oertzen, A. S. Mikhailov, H. H. Rotermund, and G. Ertl, "Subsurface oxygen in the CO oxidation reaction on Pt(110): Experiments and modeling of pattern formation," J. Phys. Chem. B **102**(25), 4966–4981 (1998).
[34]M. A. van Spronsen, J. W. M. Frenken, and I. M. N. Groot, "Observing the oxidation of platinum," Nat. Commun. **8**(1), 429 (2017).
[35]H. P. Bonzel and R. Ku, "Mechanisms of the catalytic carbon monoxide oxidation on Pt (110)," Surf. Sci. **33**(1), 91–106 (1972).
[36]C. E. Wartnaby, A. Stuck, Y. Y. Yeo, and D. A. King, "Calorimetric measurement of catalytic surface reaction heat: CO oxidation on Pt{110}," J. Chem. Phys. **102**(4), 1855–1858 (1995).
[37]R. E. Winans, S. Vajda, B. Lee, S. J. Riley, S. Seifert, G. Y. Tikhonov, and N. A. Tomczyk, "Thermal stability of supported platinum clusters studied by in situ GISAXS," J. Phys. Chem. B **108**(47), 18105–18107 (2004).
[38]J. Wang, E. Sauter, A. Nefedov, S. Heißler, F. Maurer, M. Casapu, J.-D. Grunwaldt, Y. Wang, and C. Wöll, "Dynamic structural evolution of Ceria-Supported Pt particles: A thorough spectroscopic study," J. Phys. Chem. C **126**(21), 9051–9058 (2022).
[39]V. Truttmann, H. Drexler, M. Stöger-Pollach, T. Kawawaki, Y. Negishi, N. Barrabés, and G. Rupprechter, "CeO_2 supported gold nanocluster catalysts for CO oxidation: Surface evolution influenced by the Ligand shell," ChemCatChem **14**(14), e202200322 (2022).
[40]S. Bonanni, K. Aït-Mansour, H. Brune, and W. Harbich, "Overcoming the strong metal−support interaction state: CO oxidation on TiO_2 (110)-Supported Pt nanoclusters," ACS Catal. **1**(4), 385–389 (2011).
[41]A. Beniya, S. Higashi, N. Ohba, R. Jinnouchi, H. Hirata, and Y. Watanabe, "CO oxidation activity of non-reducible oxide-supported mass-selected few-atom Pt single-clusters," Nat. Commun. **11**(1), 1888 (2020).
[42]Y. Lu, C. Thompson, D. Kunwar, A. K. Datye, and A. M. Karim, "Origin of the high CO oxidation activity on CeO_2 supported Pt nanoparticles: Weaker binding of CO or facile oxygen transfer from the support?," ChemCatChem **12**(6), 1726–1733 (2020).
[43]F. Maurer, J. Jelic, J. Wang, A. Gänzler, P. Dolcet, C. Wöll, Y. Wang, F. Studt, M. Casapu, and J.-D. Grunwaldt, "Tracking the formation, fate and consequence for catalytic activity of Pt single sites on CeO_2," Nat. Catal. **3**(10), 824–833 (2020).
[44]P. Dolcet, F. Maurer, M. Casapu, and J.-D. Grunwaldt, "Insights into the structural dynamics of Pt/CeO_2 single-site catalysts during CO oxidation," Catalysts **11**(5), 617 (2021).
[45]C.-H. Chung, F.-Y. Tu, T.-A. Chiu, T.-T. Wu, and W.-Y. Yu, "Critical roles of surface oxygen vacancy in heterogeneous catalysis over Ceria-based materials: A selected review," Chem. Lett. **50**(5), 856–865 (2021).
[46]A. I. Stadnichenko, E. M. Slavinskaya, O. A. Stonkus, and A. I. Boronin, "Low-temperature CO oxidation by the Pt/CeO_2 based catalysts," ChemCatChem **16**(15), e202301727 (2024).
[47]E. Bêche, P. Charvin, D. Perarnau, S. Abanades, and G. Flamant, "Ce 3d XPS investigation of cerium oxides and mixed cerium oxide ($Ce_xTi_yO_z$)," Surf. Interface Anal. **40**(3–4), 264–267 (2008).
[48]E. Paparazzo, "On the curve-fitting of XPS Ce(3d) spectra of cerium oxides," Mater. Res. Bull. **46**(2), 323–326 (2011).
[49]D. J. Morgan, "Photoelectron spectroscopy of ceria: Reduction, quantification and the myth of the vacancy peak in XPS analysis," Surf. Interface Anal. **55**(11), 845–850 (2023).
[50]N. Yigit, A. Genest, S. Terloev, J. Möller, and G. Rupprechter, "Active sites and deactivation of room temperature CO oxidation on Co_3O_4 catalysts: Combined experimental and computational investigations," J. Phys. Condens. Matter **34**(35), 354001 (2022).
[51]B. Nan, Q. Fu, J. Yu, M. Shu, L.-L. Zhou, J. Li, W.-W. Wang, C.-J. Jia, C. Ma, J.-X. Chen, L. Li, and R. Si, "Unique structure of active platinum-bismuth site for oxidation of carbon monoxide," Nat. Commun. **12**(1), 3342 (2021).
[52]H. Wang, J.-X. Liu, L. F. Allard, S. Lee, J. Liu, H. Li, J. Wang, J. Wang, S. H. Oh, W. Li, M. Flytzani-Stephanopoulos, M. Shen, B. R. Goldsmith, and M. Yang, "Surpassing the single-atom catalytic activity limit through paired Pt-O-Pt ensemble built from isolated Pt1 atoms," Nat. Commun. **10**(1), 3808 (2019).

[53]M. Cargnello, V. V. T. Doan-Nguyen, T. R. Gordon, R. E. Diaz, E. A. Stach, R. J. Gorte, P. Fornasiero, and C. B. Murray, "Control of metal nanocrystal size reveals metal-support interface role for Ceria catalysts," Science **341**(6147), 771–773 (2013).
[54]J. Reich, S. Kaiser, U. Heiz, J.-D. Grunwaldt, M. M. Kappes, F. Esch, and B. A. J. Lechner, "A critical view on the quantification of model catalyst activity," Top. Catal. **67**(13–14), 880–891 (2024).
[55]T. Schedlbauer, P. Lott, M. Casapu, H. Störmer, O. Deutschmann, and J.-D. Grunwaldt, "Impact of the support on the catalytic performance, inhibition effects and SO_2 poisoning resistance of Pt-based formaldehyde oxidation catalysts," Top. Catal. **62**(1–4), 198–205 (2019).
[56]M. Casapu, A. Fischer, A. M. Gänzler, R. Popescu, M. Crone, D. Gerthsen, M. Türk, and J.-D. Grunwaldt, "Origin of the normal and inverse hysteresis behavior during CO oxidation over Pt/Al_2O_3," ACS Catal. **7**(1), 343–355 (2017).
[57]A. M. Gänzler, M. Casapu, P. Vernoux, S. Loridant, F. J. Cadete Santos Aires, T. Epicier, B. Betz, R. Hoyer, and J. Grunwaldt, "Tuning the structure of platinum particles on Ceria in situ for enhancing the catalytic performance of exhaust gas catalysts," Angew. Chem. Int. Ed. **56**(42), 13078–13082 (2017).
[58]A. M. Gänzler, M. Casapu, F. Maurer, H. Störmer, D. Gerthsen, G. Ferré, P. Vernoux, B. Bornmann, R. Frahm, V. Murzin, M. Nachtegaal, M. Votsmeier, and J.-D. Grunwaldt, "Tuning the Pt/CeO_2 interface by in situ variation of the Pt particle size," ACS Catal. **8**(6), 4800–4811 (2018).